

Supporting Information

Unraveling the Role of Earth-abundant Fe in Suppression of Jahn–Teller Distortion of P'2-type Na_{2/3}MnO₂: Experimental and Theoretical Studies

Ji Ung Choi[†], Yun Ji Park[†], Jae Hyeon Jo[†], Liang-Yin Kuo[‡], Payam Kaghazchi^{,‡} and Seung-Taek Myung^{*,†}*

[†]*Department of Nanotechnology and Advanced Materials Engineering, Sejong University, Seoul 05006, South Korea*

[‡]*Institut für Chemie und Biochemie, Freie Universität Berlin, Takustr. 3, Berlin 14195, Germany & Forschungszentrum Jülich GmbH, Institute of Energy and Climate Research (IEK-1), Materials Synthesis and Processing, Wilhelm-Johnen-Straße, 52425, Jülich, Germany*

*Corresponding author. E-mail: payamk@zedat.fu-berlin.de (Payam Kaghazchi); smyung@sejong.ac.kr (S.-T. Myung)

EXPERIMENTAL

Material synthesis

$\text{Na}_{2/3}[\text{Fe}_x\text{Mn}_{1-x}]\text{O}_2$ [$x=0, 0.11, 0.22$] compounds were prepared using a simple combustion method. An aqueous solution was stoichiometrically prepared by dissolving $\text{Mn}(\text{NO}_3)_2 \cdot 6\text{H}_2\text{O}$, NaNO_3 , $\text{Fe}(\text{NO}_3)_3 \cdot 9\text{H}_2\text{O}$, citric acid, and sucrose in distilled water and continuously adding an aqueous citric acid solution and sucrose to achieve a nitrates: citric acid: sucrose weight ratio of 1:0.5:0.02. The solution was heated on a hot plate at 120 °C overnight under constant stirring to evaporate the solvent. The dried powders were then further heated to 200 °C to induce auto-combustion. The obtained powders were pelletized and calcined in a furnace at 1200 °C for 10 h in air and then slowly cooled to room temperature. The synthesized samples were analyzed using X-ray diffraction (XRD; PANalytical X'Pert, Empyrean), and the chemical compositions were determined using inductively coupled plasma-optical emission spectroscopy (ICP-OES; OPTIMA 8300 PerkinElmer). The crystal structures were analyzed using the Rietveld refinement program Fullprof.¹ The particle morphologies and sizes were evaluated using scanning electron microscopy (SEM; JXA-8100, JEOL) and high-resolution transmission electron microscopy (HR-TEM, JEM-3010, JEOL). To measure the direct current (DC) electrical conductivity, we used the direct volt-ampere method (CMT-SR1000, IT), where disc samples were contacted with a four-point probe.

Electrochemical characterization

The electrochemical properties of the samples were determined using R2032-type coin cells. Electrodes were fabricated from a mixture of the active powder (85 wt.%), KS-6 and Super-P (7.5 wt.%), and polyvinylidene fluoride (PVDF) in *N*-methyl-2-pyrrolidone (7.5 wt.%).

The prepared slurry was cast on aluminum foil and dried overnight at 110°C in a vacuum oven. The electrolyte was 0.5 M NaPF₆ in a mixture of propylene carbonate (PC) and fluoroethylene carbonate (FEC) in a 98:2 volume ratio.² The fabricated cells were tested in the voltage range of 1.5–4.3 V at a rate of C/10 (26 mA g⁻¹) at 25 °C. AC impedance measurements were performed in the 1 MHz–1 mHz frequency range with an AC amplitude of 10 mV.

Density Functional theory (DFT) calculations

The atomic structures of various possible configurations of Na_{2/3}MnO₂ and their Coulomb energies (calculated using the Ewald summation algorithm) were determined using the so-called *supercell* code.³ DFT calculations were performed using the projector-augmented plane-wave (PAW) method as implemented in the Vienna *Ab Initio* Simulation Package (VASP).⁴ The Perdew–Burke–Ernzerhof (PBE) functional⁵ with the on-site Coulomb interaction correction introduced by Dudarev *et al.*⁶ was utilized. To model the bare and Fe-doped Na_{2/3}MnO₂, we used a 3×3×1 unit cell with a Monkhorst–Pack *k*-point mesh of 2×1×2 and energy cut-off of 500 eV. To compute the total energies of possible favorable structures of Na_{2/3}MnO₂ that were determined based on the Coulomb energy values, we performed DFT-PBE+U calculations with a U–J value of 4.0 for Mn. To determine appropriate values of U–J for Mn and Fe that give reasonable results for the doping-induced lattice parameter change, we studied the effect of the U–J value on the *a*, *b*, and *c* lattice sizes as well as the J–T distortion for bare as well as 11% and 22% Fe-doped Na_{2/3}MnO₂ (**Figures S3 and S4**). A U–J value of 6.0 for both Mn and Fe provided reasonable results compared with our experimental XRD data.

Structural study

The structures of the samples during cycling were examined using *ex situ* and *operando* synchrotron XRD (SXRD) and *ex situ* X-ray absorption spectroscopy (XAS). *Operando* SXRD and *ex situ* XAS measurements were performed at beamlines 9B (Source = synchrotron light, $\lambda = 0.8265 \text{ \AA}$) and 8C, respectively, of the Pohang Accelerator Laboratory (PAL), Pohang, South Korea. The SXRD data were converted to Cu wavelength ($\lambda = 1.5406 \text{ \AA}$) for convenience. The raw XAS data were corrected for pre-edge and post-edge background and normalized to unit step height. The X-ray absorption near-edge structure (XANES) data were analyzed using the Athena software package.⁷ The effects of the phase stability and redox behaviors during cycling are discussed based on these results.

Thermal property

For differential scanning calorimetry (DSC) analysis, the R2032 coin-type cells were fully charged to 4.3 V and disassembled in a glove box, and the electrodes were rinsed in salt-free dimethyl carbonate for 1 day. After the remaining electrolyte was carefully removed from the electrode surface, the cathode materials were recovered from the current collector. A stainless-steel sealed pan with a gold-plated copper seal was used to collect 3–5 mg samples. These measurements were performed in a Pyris 1 calorimeter (Perkin-Elmer) at a temperature ramp rate of $1 \text{ }^\circ\text{C min}^{-1}$. The weight was constant in all cases, indicating that no leaks occurred during the experiments.

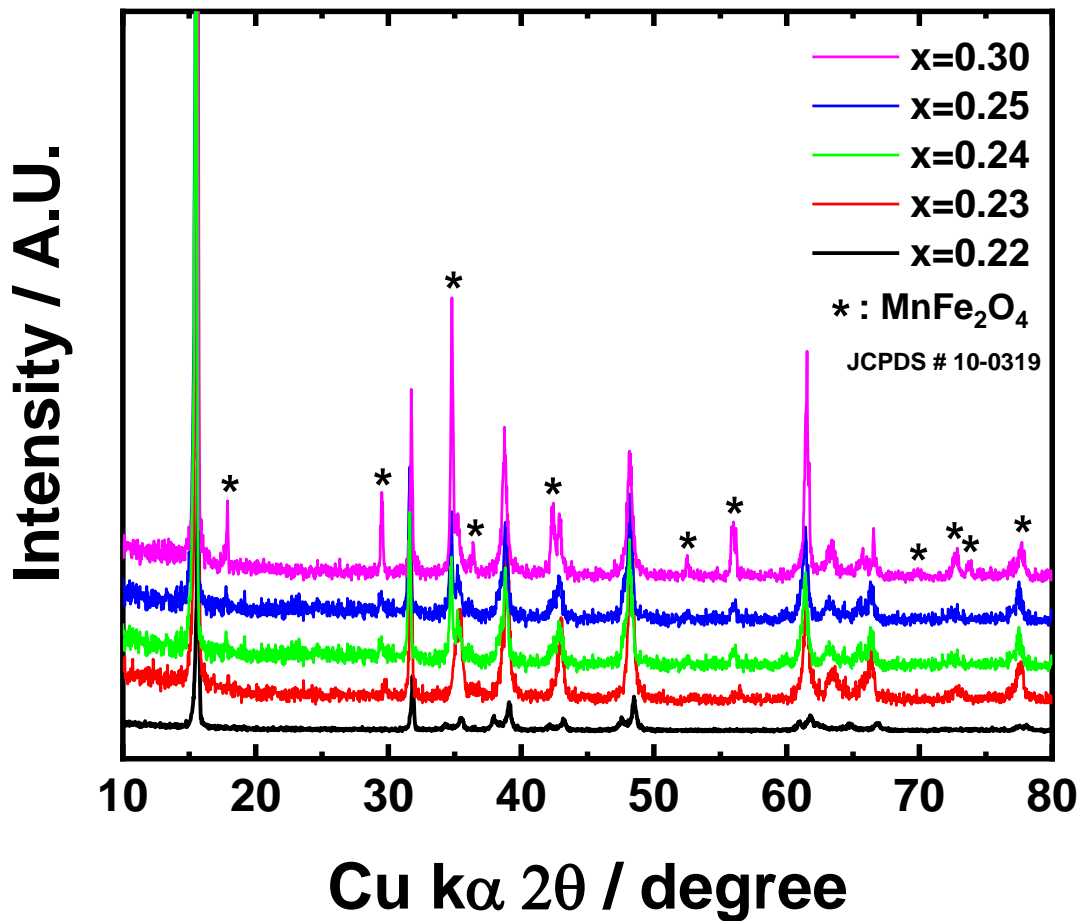


Figure S-1. XRD patterns of the $\text{Na}_{2/3}[\text{Fe}_x\text{Mn}_{1-x}]\text{O}_2$ ($0.22 \leq x \leq 0.3$) compounds with different Fe-substitution ratio with MnFe_2O_4 reference.

To confirm the soluble range of Fe in P'2-type $\text{Na}_{2/3}[\text{Mn}_{1-x}\text{Fe}_x]\text{O}_2$, the addition of Fe was increased to 30% of the Mn content (**Figure S-1**). The MnFe_2O_4 phase appeared for Fe contents greater than 22%, indicating that a solid solution is formed up to $x = 0.22$ in $\text{Na}_{2/3}[\text{Mn}_{1-x}\text{Fe}_x]\text{O}_2$.

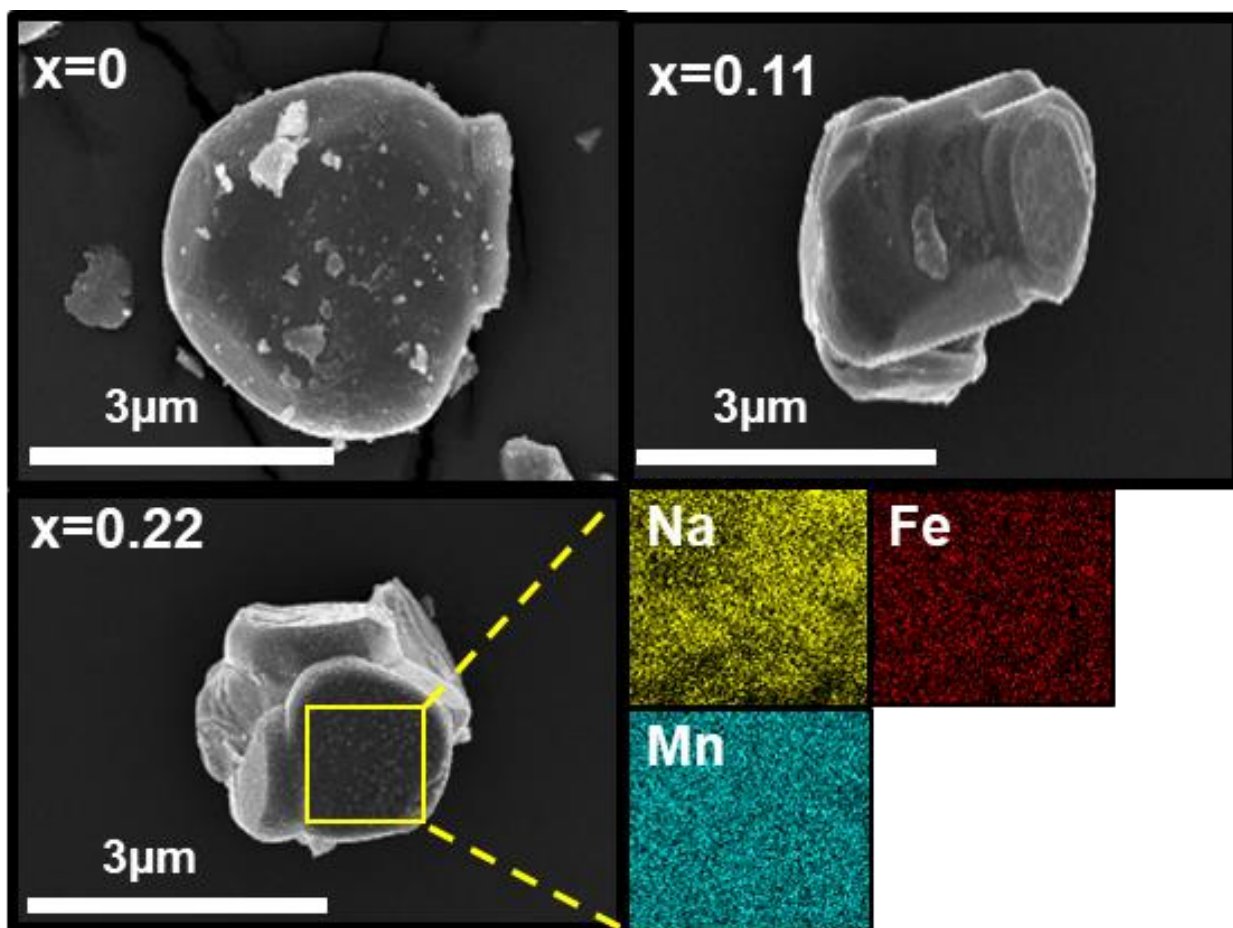


Figure S-2. SEM image with EDX maps of Na, Fe, Mn of $\text{Na}_{2/3}[\text{Fe}_x\text{Mn}_{1-x}]\text{O}_2$ ($x=0, 0.11, \text{ and } 0.22$) samples.

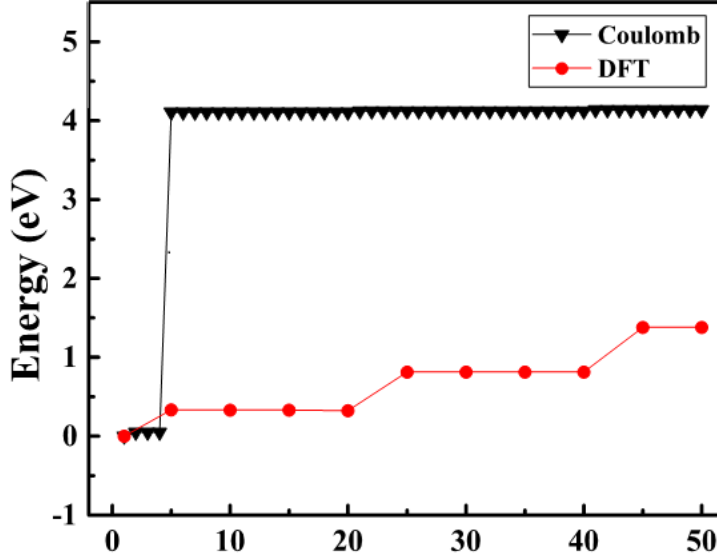


Figure S-3. Coulomb energies of the top 50 low-energy structures of $\text{Na}_{2/3}\text{MnO}_2$ as well as DFT-PBE+U total energies of several low-energy structures. Both the Coulomb and DFT energies are referenced to their lowest values.

To find the minimum-energy structure of bare $\text{Na}_{2/3}\text{MnO}_2$, we determined the arrangement of Na ions in Na sites. We focused on a $3 \times 3 \times 1$ unit cell, for which 24 of the 36 prismatic sites should be occupied by Na ions. To reduce the number of possible configurations, the positions of 4 Na ions were fixed at 4 homogeneously separated prismatic sites. The Coulomb energies of all the possible arrangements of the remaining 20 Na ions in the remaining unoccupied 32 prismatic sites ($\frac{32!}{20!12!} = 225792840$) were then calculated. To maintain charge neutrality, we considered the following charges for the ions: Na: +1.5, Mn: +3, O: -2. In fact, Na cations should have a charge value of +1, and Mn cations should have either a charge value of +3 or +4 depending on the arrangement of nearest neighbor Na cations and vacancies (V_{Na}^-). Finding the minimum-energy structure of $\text{Na}_{2/3}\text{MnO}_2$ with a favorable arrangement of $\text{Mn}^{+3}/\text{Mn}^{+4}$ and $\text{Na}^+/V_{\text{Na}}^-$ is a formidable task since we have to explore a huge number of possible structures of more than 10^8 , which is beyond the capability of the Supercell program by which we created different configurations. We, therefore, had to choose a charge of +1.5 for Na and +3.0 for Mn. Since the determined structure of $\text{Na}_{2/3}\text{MnO}_2$ from the Coulomb energy analysis is in agreement with that from DFT calculation, we believe that this charge assignment is reasonable. The Coulomb energies of the first 50 favorable configurations and the corresponding total energies (determined using the DFT-PBE+U calculations) of 11 structures from the 50 configurations are shown in **Figure S-3**.

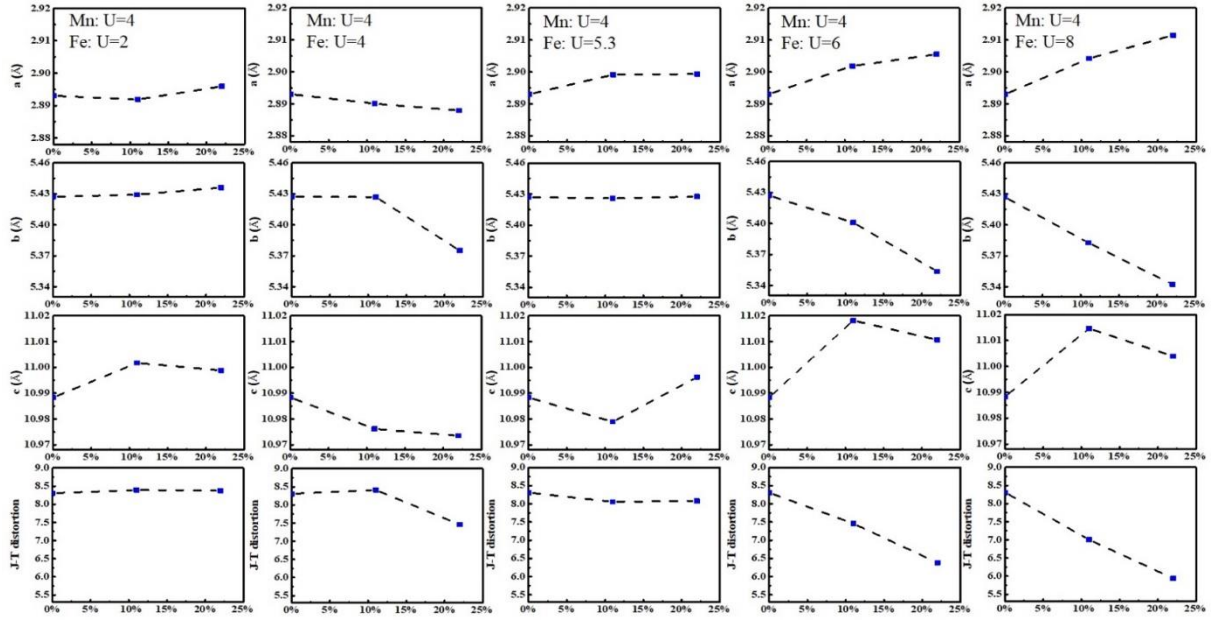


Figure S-4. DFT-PBE+U-calculated lattice parameters and J-T distortion in $\text{Na}_{2/3}\text{MnO}_2$ as function of level of Fe doping with different U-J values of Fe. The U-J value of Mn was fixed to 4.0.

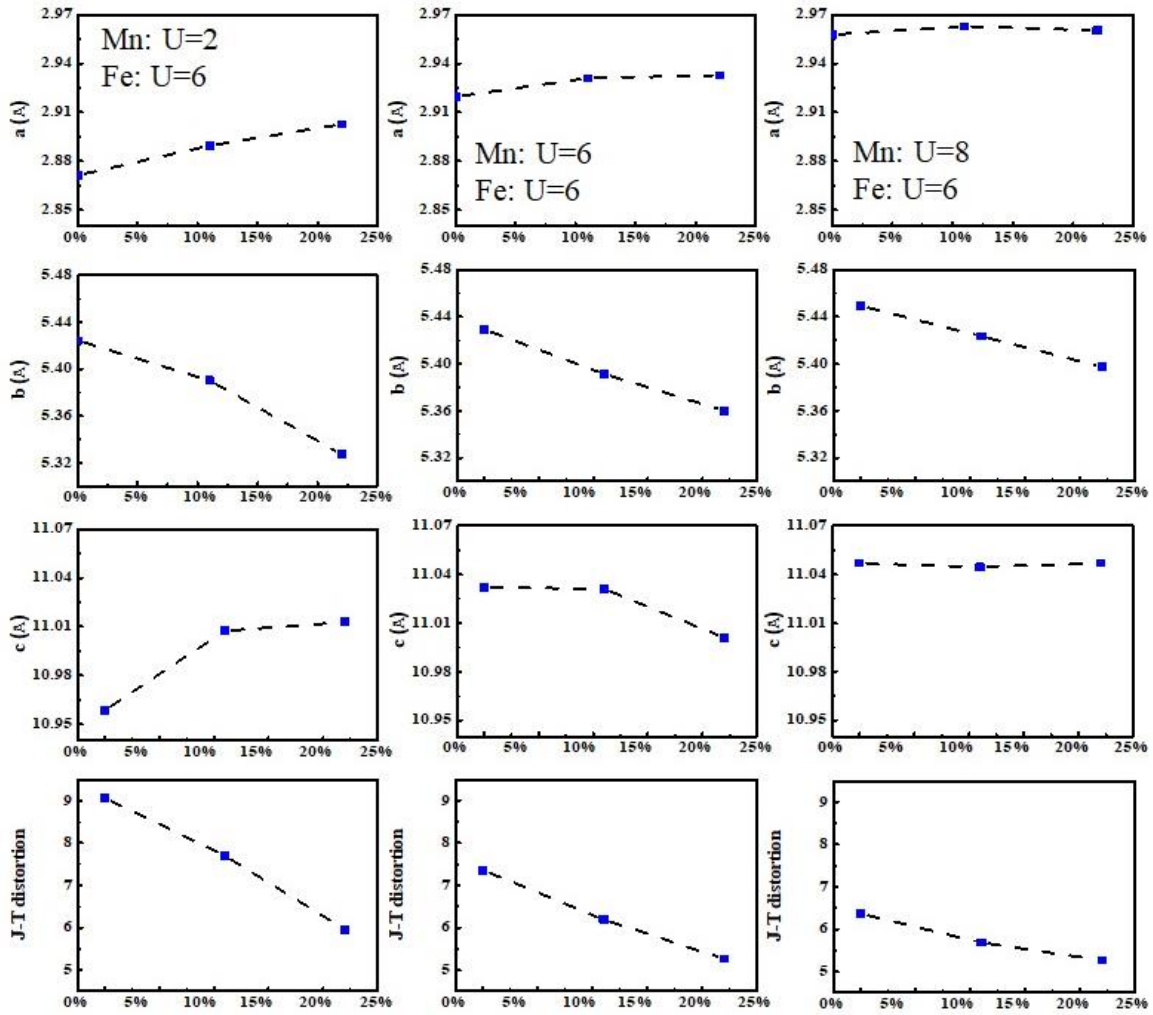


Figure S-5. DFT-PBE+U-calculated lattice parameters and J-T distortion in $\text{Na}_{2/3}\text{MnO}_2$ as function of level of Fe doping with different U-J values of Mn. The U-J value of Fe was fixed to 6.0 based on the results of **Figure S-4**.

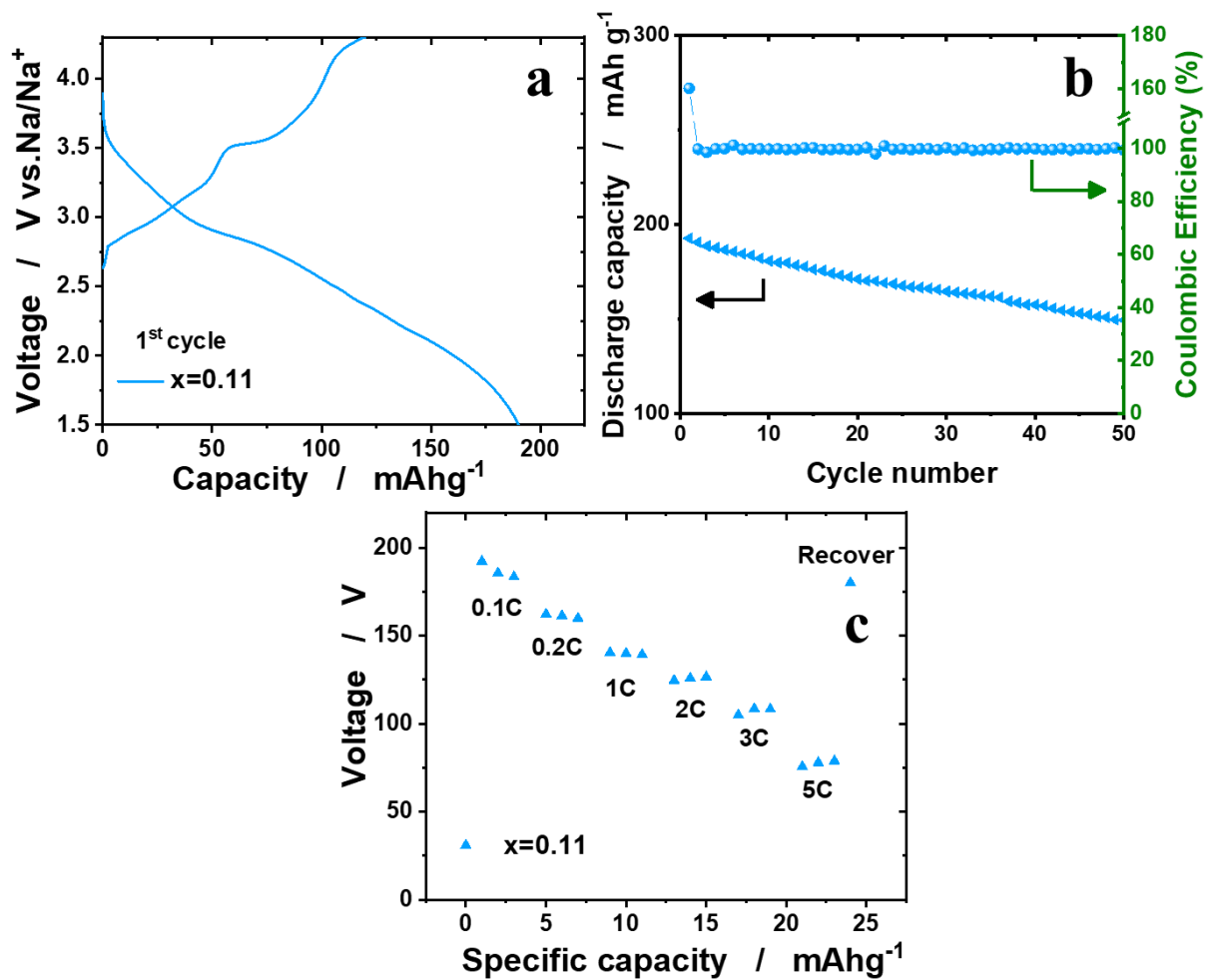
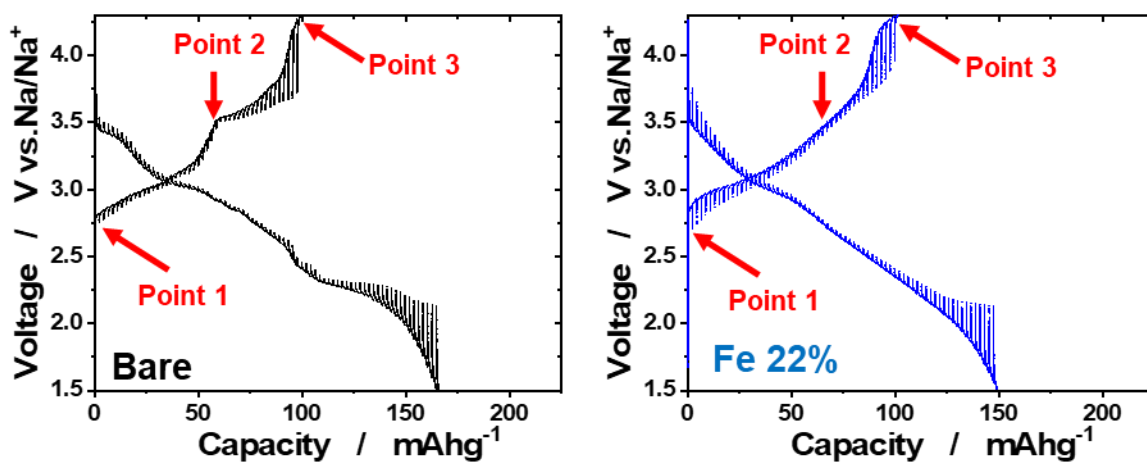


Figure S-6. (a) Galvanostatic charge/discharge voltage profiles, (b) cycling performance at 0.1C (26 mA g⁻¹) and (c) resulting rate capability of $\text{Na}_{2/3}[\text{Fe}_{0.11}\text{Mn}_{0.89}]\text{O}_2$ electrode.



D_{Na^+} ($cm^2 s^{-1}$)	Point 1 ($\delta=0.043$)	Point 2 ($\delta=0.427$)	Point 3 ($\delta=0.666$)
Bare	1.23×10^{-13}	1.31×10^{-14}	2.13×10^{-17}
Fe 22%	5.37×10^{-11}	2.09×10^{-12}	4.39×10^{-15}

Figure S-7. GITT results of $Na_{2/3}[Fe_{0.22}Mn_{0.78}]O_2$ ($x=0, 0.22$) electrodes.

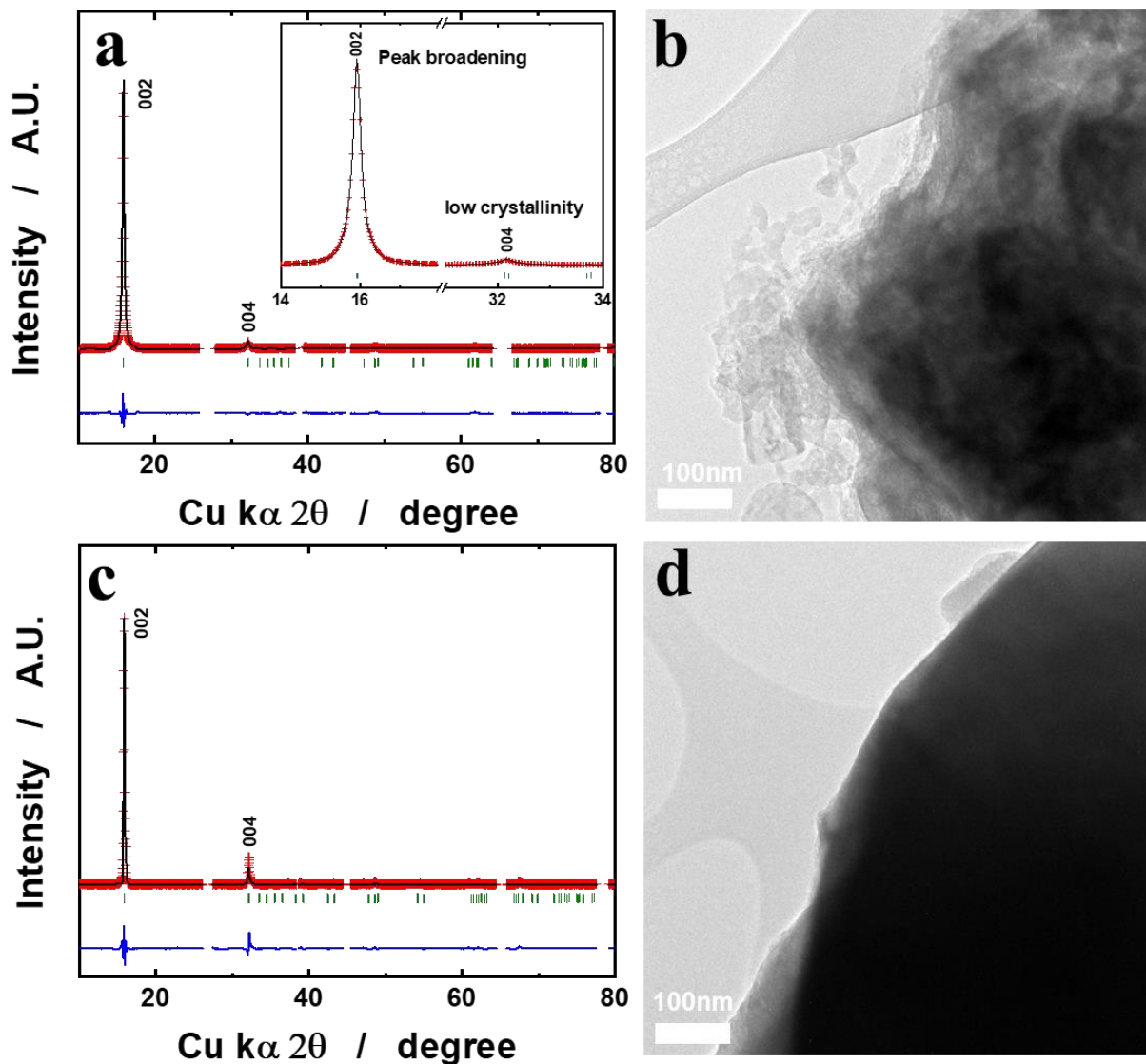


Figure S-8. *ex-situ* XRD and HRTEM images of (a,b) after 50 cycled $\text{Na}_{2/3}\text{MnO}_2$ and (c,d) after 100 cycled $\text{Na}_{2/3}[\text{Fe}_{0.22}\text{Mn}_{0.78}]\text{O}_2$ electrodes.

The sharp feature of the (002) and (004) peaks still remained (**Figure S-8c**), and the particle was not greatly damaged even after 100 cycles (**Figure S-8d**). It is also interesting that compared with that of $\text{P}'2\text{-Na}_{2/3}\text{MnO}_2$, the lattice was less varied even after prolonged cycling (**Figure S-8a and S-8b**). This finding indicates that the biphasic reaction was suppressed by the introduction of Fe in $\text{Na}_{2/3}[\text{Fe}_{0.22}\text{Mn}_{0.78}]\text{O}_2$.

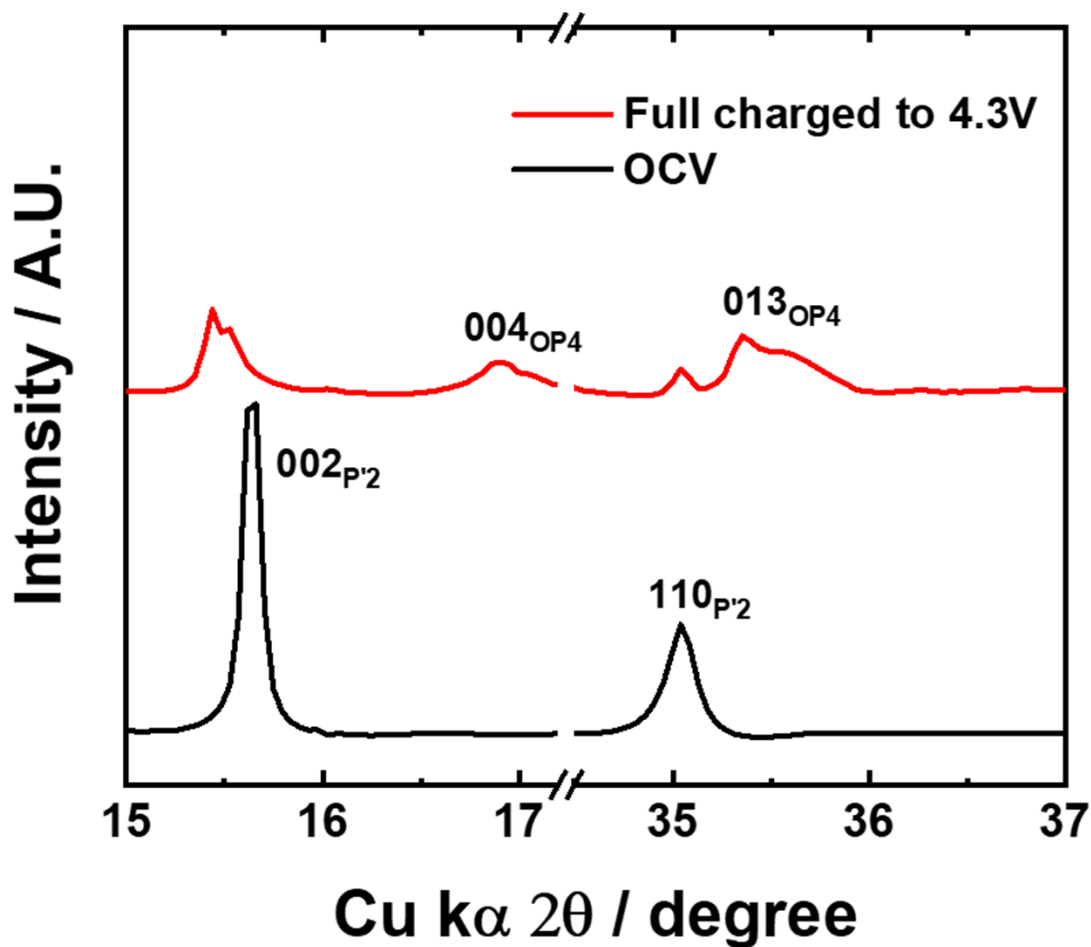


Figure S-9. XRD patterns of $\text{Na}_{2/3}[\text{Fe}_{0.22}\text{Mn}_{0.78}]\text{O}_2$ electrodes for OCV (Black) and Full charged to 4.3 V (Red) from *Operando* SXR patterns.

In the case of the $\text{Na}_{2/3}[\text{Fe}_{0.22}\text{Mn}_{0.78}]\text{O}_2$ electrode, the P'2 is transformed to OP4 on charge (desodiation), and it moves like $\text{OP4} \rightarrow \text{P}'2 \rightarrow \text{P}''2$ for the P'2 $\text{Na}_{2/3}\text{MnO}_2$ but a simpler transition is seen for the P'2 $\text{Na}_{2/3}[\text{Fe}_{0.22}\text{Mn}_{0.78}]\text{O}_2$ followed by $\text{OP4} \rightarrow \text{P}'2$ on discharge (sodiation). As shown in **Figure S-9**, such OP4 phase is clearly observed in the in situ XRD pattern.

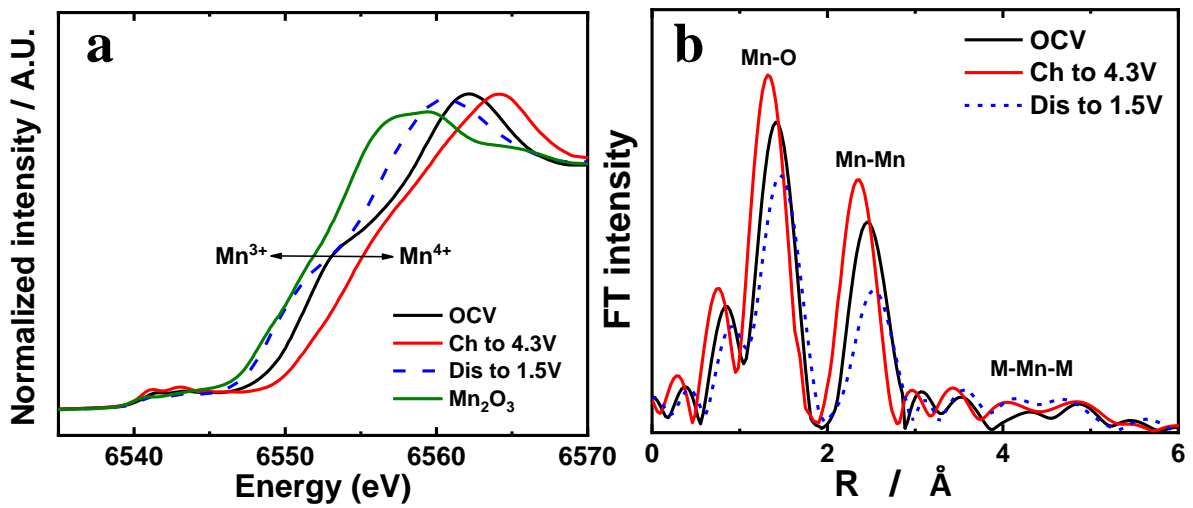


Figure S-10. XANES spectra at the (a) the Mn and the K^3 -weighted Fourier transform magnitudes of the (b) the Mn for $\text{Na}_{2/3}\text{MnO}_2$ electrode during the sodium intercalation process.

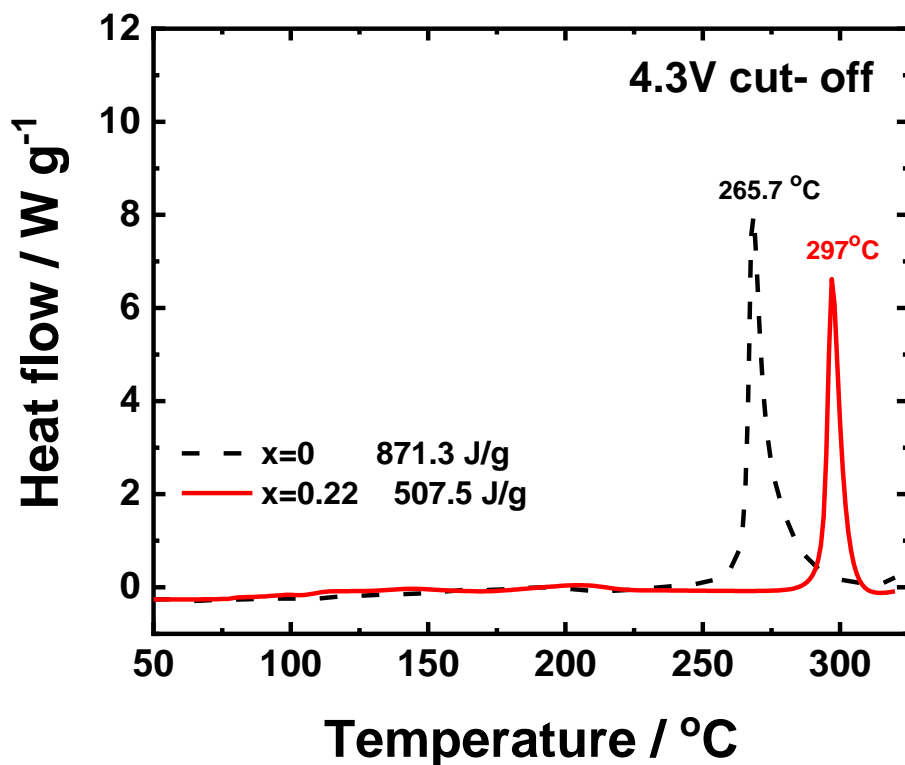


Figure S-11. DSC curves of $\text{Na}_{2/3}[\text{Fe}_x\text{Mn}_{1-x}]\text{O}_2$ ($x=0$ and 0.22) electrodes charged to 4.3V .

Figure S-11 presents the DSC curves for desodiated $\text{Na}_{0.18}\text{MnO}_2$ and $\text{Na}_{0.18}[\text{Fe}_{0.22}\text{Mn}_{0.78}]\text{O}_2$ electrodes obtained after charging to 4.3V . The onset temperature of the exothermic reaction shifted from 238 °C to 281 °C with the introduction of Fe in the crystal structure, which further raised the main reaction temperature from 265 °C to 297 °C . Hence, the Fe substitution delays the destructive exothermic reaction with substantially reduced heat generation.

Table S-1. Summary of refined crystallographic parameters, degree of distortion and electric conductivity of $\text{Na}_{2/3}[\text{Fe}_x\text{Mn}_{1-x}]\text{O}_2$ ($x=0, 0.11, \text{ and } 0.22$) compounds.

Compound	Atom	x	y	z	B	occ	$R_{wp} / \%$	Electric conductivity (Scm^{-1})
x=0	Na	0	0.068	0.25	3.16	0.215	13.4%	6.09×10^{-6} S cm^{-1}
	Na	0	0.312	0.25	1.5	0.455		
	Mn	0	0	0	0.273	1.0		
	O	0	0.651	0.097	0.728	1.0		
	a(Å)	2.8301(5)	b(Å)	5.2752(1)	c(Å)	11.1971(1)	Distortion	7.0%
x=0.11	Na	0	0.081	0.25	3.5	0.213	14.7%	2.09×10^{-5} S cm^{-1}
	Na	0	0.330	0.25	2.217	0.452		
	Mn	0	0	0	0.42	0.89		
	Fe	0	0	0	0.42	0.11		
	O	0	0.668	0.089	0.85	1.0		
a(Å)	2.8405(9)	b(Å)	5.2602(9)	c(Å)	11.1801(2)	Distortion	6.46%	
x=0.22	Na	0	0.084	0.25	3.5	0.205	10.5%	1.11×10^{-4} S cm^{-1}
	Na	0	0.335	0.25	2.2	0.447		
	Mn	0	0	0	0.4	0.78		
	Fe	0	0	0	0.4	0.22		
	O	0	0.654	0.090	0.85	1.0		
a(Å)	2.8708(1)	b(Å)	5.2141(1)	c(Å)	11.1719(5)	Distortion	4.63%	

Table S-2. Lattice parameters obtained from Rietveld refinement after extensively cycled electrodes.

After extensive cycled							
$\text{Na}_{2/3}[\text{Fe}_x\text{Mn}_{1-x}]\text{O}_2$ electrodes	Atom	x	y	z	B	Occ	$R_{\text{wp}} / \%$
x=0	Na	0	-0.066	0.25	3.154	0.179	
	Na	0	0.3321	0.25	1.383	0.358	
	Mn	0	0.0	0.0	0.27	1.0	11.2%
	O	0	0.6878	0.9040	0.73	1.0	
	a(Å)	2.8728(2)	b(Å)	5.3156(1)	c(Å)	11.1312(8)	
x=0.22	Na	0.0	-0.084	0.25	3.5	0.203	
	Na	0.0	0.335	0.25	2.2	0.407	
	Mn	0.0	0.0	0.0	0.4	0.78	14.1%
	Fe	0.0	0.0	0.0	0.4	0.22	
	O	0.0	0.6694	0.8931	1.0	1.0	
	a(Å)	2.8907(1)	b(Å)	5.2297(3)	c(Å)	11.1709(7)	

Table S-3. ICP-AAS results of Mn dissolution obtained from extensively cycled cells.

After extensive cycled $\text{Na}_{2/3}[\text{Fe}_x\text{Mn}_{1-x}]\text{O}_2$ electrodes	Mn concentration in electrolyte (ppm)
x=0	92 ppm
x=0.22	36 ppm

REFERENCES

- (1) Roisnel, T.; Rodriguez-Carjaval, J.; Fullprof Manual, Institut Laue-Langevin, Grenoble, France, **2002**.
- (2) Komaba, S.; Ishikawa, T.; Yabuuchi, N.; Murata, W.; Ito, A.; Ohsawa, Y. Fluorinated Ethylene Carbonate as Electrolyte Additive for Rechargeable Na Batteries. *ACS Appl. Mater. Interfaces* **2011**, *3*, 4165-4168.
- (3) Okhotnikov, K.; Charpentier, T.; Cadars, Supercell program: a combinatorial structure-generation approach for the local-level modeling of atomic substitutions and partial occupancies in crystals. *S. Journal of Cheminformatics* **2016**, *8*, 17
- (4) Kresse, G.; Furthmuller, Efficient iterative schemes for ab initio total-energy calculations using a plane-wave basis set. *J. Phys. Rev. B: Condens. Matter Mater. Phys.* **1996**, *54*, 11169.
- (5) Perdew, J. P.; Burke, K.; Ernzerhof, Generalized Gradient Approximation Made Simple. *M. Phys. Rev. Lett.* **1996**, *77*, 3865.
- (6) Dudarev, S. L.; Botton, G. A.; Savrasov, S. Y.; Humphreys, C. J.; Sutton, A. P. Electron-energy-loss spectra and the structural stability of nickel oxide: An LSDA1U study. *Phys. Rev.B: Condens. Matter Mater. Phys.* **1998**, *57*, 1505.
- (7) Ravel, B.; Newville, M.; Athena, Artemis, Hephaestus, J. *Synchrotron Radiat.* **2005**, *12*, 537.